

The DESI PRObabilistic Value-Added Bright Galaxy Survey (PROVA-BGS) Mock Challenge

CHANGHOON HAHN,¹ GYUBIN KWON, MALGORZATA SIUDEK, RITA TOJEIRO, AND GQP WG

¹*Department of Astrophysical Sciences, Princeton University, Peyton Hall, Princeton NJ 08544, USA*

ABSTRACT

In this project, we present the methodology for inferring physical properties of galaxies from joint SED fitting of the DESI optical photometry and spectroscopy. We construct realistic forward modeled DESI data from star formation and chemical enrichment histories of galaxies in the L-GALAXIES semi-analytic model and the ILLUSTRIS TNG hydrodynamic simulations. Then, using these mock observations, we demonstrate that the stellar mass and SFR posteriors from our SED fitting are consistent with constraints from other SED fitting methods in the literature and, more importantly, the input stellar masses and SFRs from the simulations. The SED fitting we present and validate in this project will be used to construct the PRObabilistic Value-Added Bright Galaxy Survey (PROVABGS) from DESI observations.

Keywords: keyword1 – keyword2 – keyword3

1. INTRODUCTION

The Dark Energy Spectroscopic Instrument will conduct the largest spectroscopic galaxy survey to date covering $\sim 14,000 \text{ deg}^2$ (?). Over the next five years,

What is DESI? Provide an overview of DESI specifics, numbers, and science goals, which will mostly be cosmology (BAO, RSD, etc). DESI will be great Beyond its impact on cosmology, DESI will also be transformative for galaxy science.

provide value-added galaxy catalogs (VAGCs), which will be transformative for galaxy science. In the past, VAGCs such as the MPA-JHU¹ provided galaxy properties from emission line analyses of SDSS spectra ?.

Similarly, the NYU-VAGC (?),

These catalogs have been indispensable for establishing the global statistical view of galaxy properties (see ?, for a review). **previous successes with value-added catalogs**

what will PROVABGS be good for? extending previous statistical analyses on SDSS to a larger sample and to higher redshift. Mention some obvious ones: stellar mass function, luminosity function, star-formation sequence. more detailed galaxy-halo connection mention some cosmological applica-

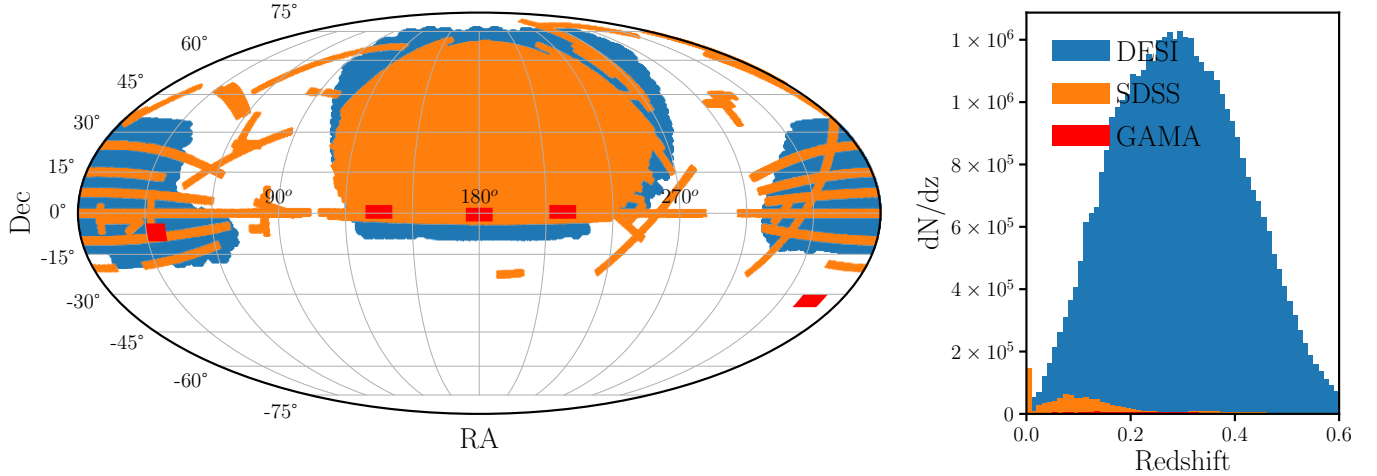


Figure 1. DESI will conduct the largest spectroscopic survey to date covering $\sim 14,000 \text{ deg}^2$. During dark time, DESI will measure >20 million spectra of luminous red galaxies, emission line galaxies, and quasars out to $z > 3$. During bright time, DESI will measure the spectra of ~ 10 million galaxies out to $z \sim 0.4$ with the Bright Galaxy Survey (BGS). *Left:* With its $\sim 14,000 \text{ deg}^2$ footprint (black), DESI will cover $\sim 2\times$ the SDSS footprint (blue; $\sim 7000 \text{ deg}^2$) and $\sim 45\times$ the GAMA footprint (orange; $\sim 300 \text{ deg}^2$). *Right:* Over this footprint, the BGS will provide spectra for a magnitude limited sample of ~ 10 million galaxies down to $r < 20$, two orders of magnitude deeper than the SDSS main galaxy sample and 0.2 mag deeper than GAMA.

tions: multi-tracer analyses. Furthermore, since BGS will measure galaxy spectra down to $r \sim 20$, we will have faint dwarf galaxies at low redshift. provabgs introduces a new frontier of low signal-to-noise statistically powerful sample that will require

Why do we need a mock challenge? We want to test and cement our methodology specifically for our GQP analysis before SV data comes out. As part of the survey preparation, we have all the tools to accurately forward model observations. **details on some of the specific tools and what we're able to simulate: realistic spectroscopy. realistic photometry. realistic spectro-photometry** All of this gives us a rare opportunity to test our methodology on bespoke simulations.

A mock challenge is also great for testing new methodology. BGS is a bright time survey and will push the boundaries of low SNR spectra. But if we can find a way to infer robust galaxy properties the statistical payout is awesome. **Something also about LRGs** We're also trying to robustly fit spectra and photometry simultaneously. This has been done before (**citations**) but not extensively tested on simulations.

2. SIMULATIONS

DESI, with its robotically-actuated and fibre-fed spectrographs, will collect 5000 spectra simultaneously. The spectra cover the wavelength range 3600 to 9800 Å, with a spectral resolution of $R = \lambda/\Delta\lambda$ between 2000 and 5500. During its five-year operation, starting in 2020, it will measure over 30 million spectra over $14,000 \text{ deg}^2$ of the sky (**cite**). In addition, these DESI targets also have optical and infrared imaging data from the DESI Legacy Imaging Surveys (hereafter Legacy Surveys **Dey et al. 2019**). The Legacy Surveys are a combination of three public projects (Dark Energy Camera

TODO

TODO

TODO

TODO

TODO

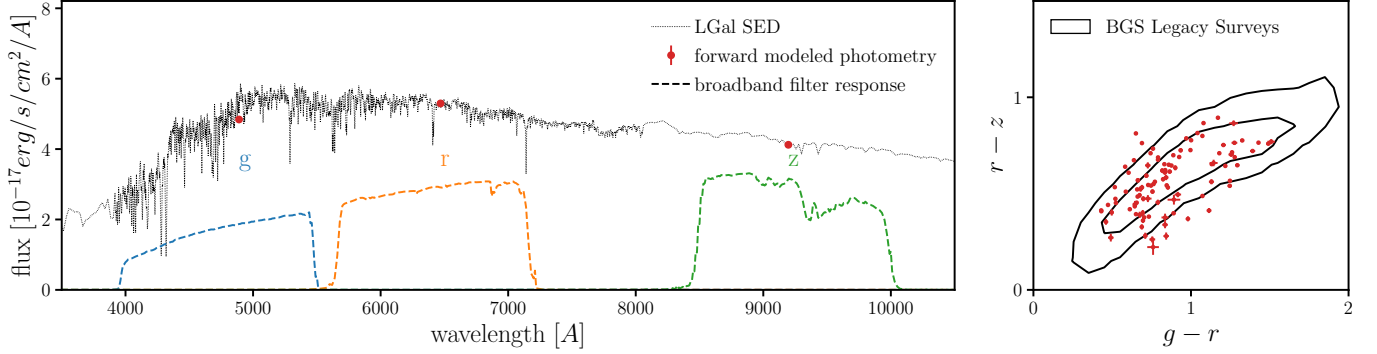


Figure 2. *Left:* We forward model DESI g , r , and z photometry (red) for our simulated galaxies (Section 2.1) by convolving their SEDs (dotted) with their broadband filters (dashed) and then applying an empirical noise model based on BGS objects in LS (Section 2.3). *Right:* The $g - r$ and $r - z$ color distribution of the forward modeled LGAL photometry is in good agreement with the color distribution of LS BGS objects (black contours).

Legacy Survey, Beijing-Arizona Sky Survey, and Mayall z -band Legacy Survey) that jointly imaged the $\sim 14,000 \text{ deg}^2$ DESI footprint in three optical bands (g , r , and z). Furthermore, DR8 of the Legacy Survey also includes photometry in the WISE $W1$, $W2$, $W3$, and $W4$ infrared bands. The infrared photometry is from all imaging through year 4 of NEOWISE-Reactivation force-photometered in the unWISE maps at the locations of Legacy Surveys optical sources (cite). Below we describe how we simulate realistic DESI-like galaxy spectra and photometry from state-of-the-art simulations.

2.1. L -Galaxies

brief overview of L-GALAXIES (hereafter LGAL; [Henriques et al. 2015](#))

2.2. Spectral Energy Distributions

For each simulated galaxy, LGAL provides the star formation histories (SFHs) and chemical enrichment histories (ZH) for its bulge and disk components separately, in approximately log-spaced lookback time bins. We treat each lookback time bin, i , as a single stellar population (SSP) of age t_i . Then, we derive the luminosities of the bulge and disk components by summing up the luminosities of all of their SSPs:

$$L^{\text{comp.}}(\lambda) = \sum_i (\text{SFH}_i^{\text{comp.}} \Delta t_i) L_{\text{SSP}}(\lambda; t_i, Z_i^{\text{comp.}}). \quad (1)$$

$\text{SFH}_i^{\text{comp.}}$ and $Z_i^{\text{comp.}}$ are the star formation rate and metallicity of the bulge or disk component in lookback time bin i . Δt_i is the width of the bin. L_{SSP} corresponds to the luminosity of the SSP, which we calculate using the Flexible Stellar Population Synthesis (FSPS [Conroy et al. 2009](#); [Conroy & Gunn 2010](#)) model. For FSPS, we use the MIST isochrones ([Paxton et al. 2011, 2013, 2015](#); [Choi et al. 2016](#); [Dotter 2016](#)), the MILES spectral library (?), and the [Chabrier \(2003\)](#) initial mass function (IMF).

Next, we apply velocity dispersions to $L^{\text{comp.}}(\lambda)$. For the disk, we apply a fixed 50 km/s velocity dispersion; for the bulge, we derive its velocity dispersion using the [Zahid et al. \(2016\)](#) empirical

TODO

relation that depends on the total bulge mass. Then, we apply dust attenuation to stellar emission in the disk component (L^{disk}) based on the cold gas content and orientation of the disk. We derive the attenuation curve using a mixed-screen model with the [Mathis \(1983\)](#) dust extinction curve. Stellar emission from stars younger than 30Myr are further attenuated with a uniform dust screen and a wavelength dependent optical depth. [@rita further details and citations for the mixed-screen model](#) No dust attenuation is applied to the bulge component. [@rita how come?](#)

TODO
TODO

Finally, we combine the attenuated disk component and the bulge component to construct the total luminosity of the simulated galaxy and then convert this rest-frame luminosity to observed-frame SED flux using its redshift, z .

$$f_{\text{SED}}(\lambda) = \frac{A(\lambda)L^{\text{disk}}(\lambda) + L^{\text{bulge}}(\lambda)}{4\pi d_L(z)^2(1+z)}. \quad (2)$$

$A(\lambda)$ is the dust attenuation for the disk component described above and $d_L(z)$ is the luminosity distance. In the left panel of Figure 2, we present an example of the SED flux constructed for an arbitrary LGALgalaxy (black).

2.3. Forward Modeling DESI Photometry

In this section, we describe how we construct realistic LS-like photometry from the SEDs of simulated galaxies described in the last section. First, we convolve the SEDs with the broadband filters of the Legacy Survey to generate broadband photometric fluxes:

$$f_X = \int f_{\text{SED}}(\lambda) R_X(\lambda) d\lambda \quad (3)$$

where f_{SED} is the galaxy SED (Eq. 2) and R_X is the transmission for filter X . We generate photometry for the g , r , and z optical bands. Next, we apply realistic measurement uncertainties to the derived photometry using a simple empirical . We match each simulated galaxy to a BGS object from LS DR9 with the nearest r -band magnitude and $g - r$ and $r - z$ color. The photometric uncertainties (σ_X) and r -band fiber flux (f_r^{fiber}) of the BGS object are then assigned to the simulated galaxy. We sample a Gaussian distribution with standard deviation σ_X and apply it to construct realistic LS-like photometry:

$$\hat{f}_X = f_X + n_X \quad \text{where } n_X \sim \mathcal{N}(0, \sigma_X). \quad (4)$$

Finally, we impose the target selection criteria of BGS ([Ruiz-Macias et al. 2021](#), Hahn *et al.* in prep.). In the left panel of Figure 2, we overplot the forward modeled photometry (red) ontop of the SED flux (black) for an arbitrary LGALgalaxy. For reference, we also plot R_X for the g , r , and z bands of the Legacy Survey in blue, orange, and green respectively. On the right panel, we compare the $g - r$ versus $r - z$ color distribution for the forward modeled LGALgalaxies (red) to the color distribution of BGS objects in LS (black contour). The forward modeled photometry show good agreement with LS BGS objects in color space.

2.4. Forward Modeling DESI Spectra

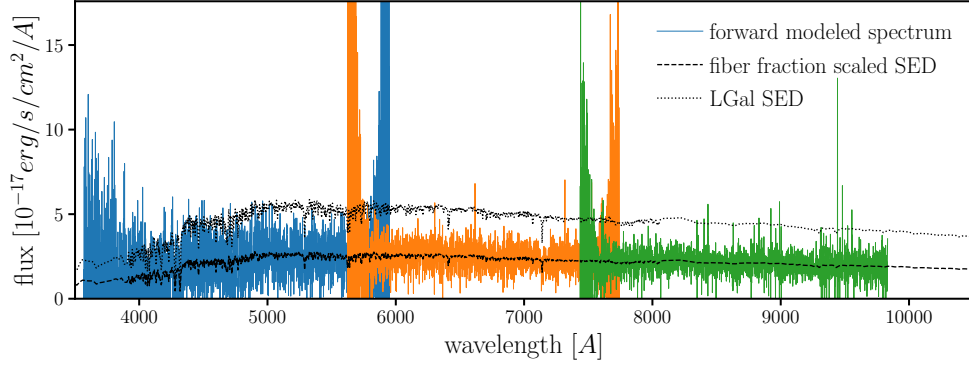


Figure 3. We construct simulated DESI spectra (solid) for LGAL simulated galaxies by applying a fiber aperture correction to the SED (dashed) and a realistic DESI noise model. We apply a fiber aperture correction by scaling down the full SED (dotted) by the r -band fiber fraction derived from the Legacy Surveys imaging. The noise model accounts for the DESI spectrograph response and an atmosphere model that accounts for the bright time observing conditions of BGS. Our forward model produces DESI-like spectra for all three arms of the DESI spectrographs: b , r , and z (blue, orange, and green, respectively). For more details, we refer readers to Section 2.4.

In this section, we describe how we construct realistic DESI-like spectroscopy from the SEDs of simulated galaxies. Our forward model involves modeling the fiber aperture effect and applying a noise model that accurately reproduces the bright time observations of BGS.

DESI uses fiber-fed spectrographs with fibers that have angular radii of $1''$. Only the light from a galaxy within this fiber aperture is collected by the instrument. LS provides measurements of photometric fiber flux within a $1''$ radius aperture (f_X^{fiber}), which estimates the flux that passed through to the fibers. When we assign photometric uncertainties to our simulated galaxies based on r , $g-r$, and $r-z$ in Section 2.3, we also assign r -band fiber flux. We model the SED flux that passes through the fiber by scaling the SED flux by the r band fiber fraction, the ratio of the r -band fiber flux over the total r band flux:

$$f^{\text{spec}}(\lambda) = \left(\frac{f_r^{\text{fiber}}}{f_r} \right) f_{\text{SED}}(\lambda). \quad (5)$$

This fiber aperture correction assumes that there is no significant color dependence. We also assume that there are no significant biases in the fiber flux measurements in LS due to miscentering of objects.

Do we want to say more about this assumption? Also cite Marta's paper investigating aperture effect.

In addition to using it for the aperture correction, we also use f_r^{fiber} to derive “measured” \hat{f}_r^{fiber} :

TODO

$$\hat{f}_r^{\text{fiber}} = f_r^{\text{fiber}} + n_r^{\text{fiber}} \quad \text{where } n_r^{\text{fiber}} \sim \mathcal{N} \left(0, \frac{f_r^{\text{fiber}}}{f_r} \sigma_r \right). \quad (6)$$

We later use \hat{f}_r^{fiber} to set the prior on the nuisance parameter of our SED modeling (Section 3).

Next, we apply a noise model that simulates the DESI instrument response and bright time observing conditions of BGS. We use the spectral simulation pipeline of **cite survey simulations**

TODO

[paper and list details](#)². More specifically, we use nominal dark time observing conditions with 180s exposure time. These conditions accurately reproduce the spectral noise and redshift success rates of observed BGS exposures in DESI survey validation data (Hahn *et al.* in prep.). In Figure 2.3, we present the forward modeled BGS spectrum of a LGAL galaxy (solid). For reference, we include the full SED (dotted) and fiber fraction scaled SED (dashed) of the galaxy.

3. JOINT SED MODELING OF PHOTOMETRY AND SPECTRA

3.1. *Stellar Population Synthesis Modeling*

PROVABGS will provide inferred galaxy properties derived from joint SED modeling of DESI photometry and spectra. For the SED modeling, we use a state-of-the-art stellar population synthesis (SPS) model that uses a non-parametric SFH with a star-burst, a non-parametric ZH that varies with time, and a flexible dust attenuation prescription.

The form of the SFH is one of the most important factors in the accuracy of an SPS model. In general, the form of the SFH requires balancing between being flexible enough to describe the wide range of SFHs in observations while not being too flexible that it can describe any SFH at the expense of constraining power. If the model SFH is not flexible enough to describe actual SFHs of galaxies, then unbiased galaxy properties cannot be inferred using the SPS model. For instance, most SPS models (*e.g.* CIGALE, [Serra et al. 2011](#); BAGPIPES, [Carnall et al. 2017](#)) use parametric SFH such as the exponentially declining τ -model. Such functional forms, however, produce biased estimates of galaxy properties (*e.g.* M_* and SFR) when used to fit mock observations of simulated galaxies ([Simha et al. 2014](#); [?](#); [Carnall et al. 2018](#)). On the other hand, many non-parametric forms of the SFH are overly flexible and allow unphysical SFHs ([Leja et al. 2019](#)), which unnecessarily increases parameter degeneracies and discards constraining power.

In our SPS model, we use a non-parametric SFH with two components: one based on non-negative matrix factorization (NMF) basis functions and a starburst component. For the first component, SFH is a linear combination of NMF SFH bases:

$$\text{SFH}^{\text{NMF}}(t, t_{\text{age}}) = \sum_{i=1}^4 \beta_i \frac{s_i^{\text{SFH}}(t)}{\int_0^{t_{\text{age}}} s_i^{\text{SFH}}(t) dt}. \quad (7)$$

$\{s_i^{\text{SFH}}\}$ are the NMF basis functions and $\{\beta_i\}$ are the coefficients. The integral in the denominator normalizes the NMF basis functions to unity. We constrain $\sum_i \beta_i = 1$, so the total SFH of the component over the age of the galaxy (t_{age}) is normalized to unity. $\{s_i^{\text{SFH}}\}$ are from Tojeiro *et al.* (in prep.) and derived from the IllustrisTNG cosmological hydrodynamic simulation ([Nelson et al. 2018](#); [Pillepich et al. 2018](#); [Springel et al. 2018](#)). The SFHs of simulated galaxies IllustrisTNG are compiled, rebinned, and smoothed [more details here](#). Afterwards, we perform non-negative matrix factorization ([Lee & Seung 1999](#); [Cichocki & Phan 2009](#); [Févotte & Idier 2011](#)) on the smooth SFHs to derive $\{s_i^{\text{SFH}}\}$. We find that 4 components is sufficient to accurately reconstruct the SFHs from IllustrisTNG.

TODO

² <https://specs.readthedocs.io>

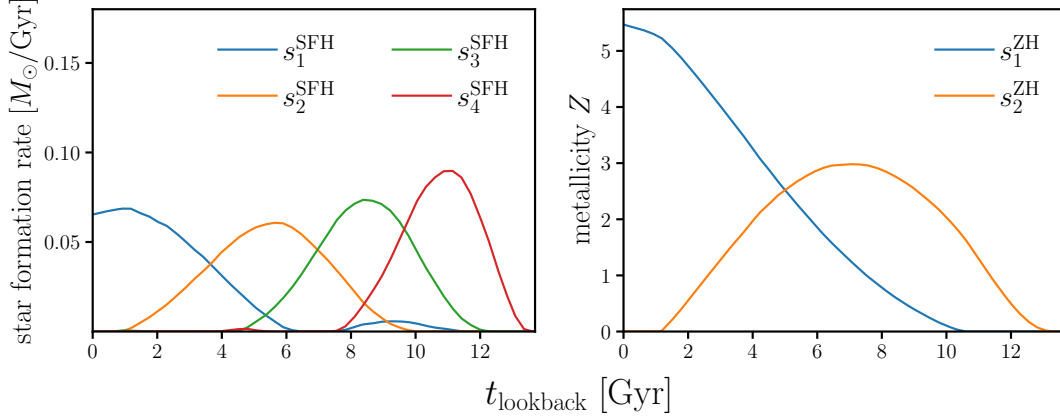


Figure 4. Non-negative matrix factorization basis functions for the SFH (left) and ZH (right). These basis functions are derived from the SFHs and ZHs of simulated galaxies in the IllustrisTNG cosmological hydrodynamic simulations.

Assuming that the SFHs of IllustrisTNG galaxies resemble the SFHs of actual observed galaxies, our NMF form provides a compact and flexible representation of the SFHs.

The NMF basis functions are derived from smooth SFHs, which means that it does not include any stochasticity. However, observations and high resolution zoom-in hydrodynamical simulations both find significant stochasticity in galaxy SFHs (Sparre et al. 2017; Caplar & Tacchella 2019; Hahn et al. 2019; Iyer et al. 2020). To include this stochasticity in our SPS model, we include a starburst component that consists of a SSP in the SFH. For the total SFH, we use

$$\text{SFH}(t, t_{\text{age}}) = (1 - f_{\text{burst}}) \text{SFH}^{\text{NMF}}(t, t_{\text{age}}) + f_{\text{burst}} \delta_{\text{D}}(t - t_{\text{burst}}). \quad (8)$$

f_{burst} is the fraction of total stellar mass formed during the starburst; t_{burst} is the time at which the starburst occurs; δ_{D} is the Dirac delta function. In total we have 6 free parameters in our SFH: 4 NMF basis coefficients (β_i), f_{burst} , and t_{burst} .

Another key part of an SPS model is the ZH, or chemical enrichment history. Current SPS models mostly assume a ZH that does not vary over time (Carnall et al. 2017; Leja et al. 2019). Since galaxies in hydrodynamical simulations and observations do not have constant metallicities throughout their history, this assumption can significantly bias the inferred galaxy properties. Instead, for our ZH, we take a similar approach to the SFH and use NMF basis functions:

$$\text{ZH}(t) = \sum_{i=1}^2 \gamma_i s_i^{\text{ZH}}(t). \quad (9)$$

$\{s_i^{\text{ZH}}(t)\}$ are the ZH NMF basis functions and $\{\gamma_i\}$ are the coefficients. $\{s_i^{\text{ZH}}(t)\}$ are fit using the ZHs of simulated galaxies from IllustrisTNG. We use two NMF components, so our ZH prescription has 2 free parameters.

Next, we use the SFH and ZH above to model the unattenuated rest-frame luminosity as a linear combination of multiple SSPs, evaluated at logarithmically-spaced lookback time bins. We use a fixed

log-binning with the bin edges starting with $(0, 10^{6.05}\text{yr})$, $(10^{6.05}, 10^{6.15}\text{yr})$, and continuing on with bins of width 0.1 dex. The binning is truncated at the age of the model galaxy. For a $z = 0$ galaxy, we use 43 t_{lookback} bins. We use log-spaced t_{lookback} bins because it better reproduces galaxy luminosities evaluated with much higher resolution t_{lookback} binning than linearly-spacing, for the same number of bins. At every t_{lookback} bin i , we evaluate the luminosity of a SSP with $\text{ZH}(t_i)$, where t_i is the center of t_{lookback} bin, and total stellar mass calculated by resampling the SFH in Eq. 8. We use FSPSto evaluate the SSP luminosities and use the MIST isochrones, MILES spectral library, and the Chabrier (2003) IMF (same as in Section 2.2). Since we use MIST isochrones, we impose a minimum and maximum limit to ZH based on its coverage: 4.49×10^{-5} and 4.49×10^{-2} , respectively. Our stellar metallicity range is significantly broader than previous studies, *e.g.* Carnall et al. (2017); Leja et al. (2017); Tacchella et al. (2021).

Before we combine the SSP luminosities, we apply dust attenuation. We use a two component Charlot & Fall (2000) dust attenuation model with birth cloud (BC) and diffuse-dust (ISM) components. The BC component represents the extra dust attenuation of young stars that are embedded in molecular clouds and HII regions. For SSPs younger than $t_i < 100\text{Myr}$, we apply the following BC dust attenuation:

$$L_i(\lambda) = L_i^{\text{unatten.}}(\lambda) \exp \left[-\tau_{\text{BC}} \left(\frac{\lambda}{5500\text{\AA}} \right)^{-0.7} \right]. \quad (10)$$

τ_{BC} is the BC optical depth that determines the strength of the BC attenuation. Afterwards, *all* SSPs are attenuated by the diffuse dust using the Kriek & Conroy (2013) attenuation curve parameterization:

$$L_i(\lambda) = L_i^{\text{unatten.}}(\lambda) \exp \left[-\tau_{\text{ISM}} \left(\frac{\lambda}{5500\text{\AA}} \right)^{n_{\text{dust}}} (k_{\text{Cal}}(\lambda) + D(\lambda)) \right]. \quad (11)$$

τ_{ISM} is the diffuse dust optical depth. n_{dust} is the ? dust index, which determines the slope of the attenuation curve. $k_{\text{Cal}}(\lambda)$ is the ? attenuation curve and $D(\lambda)$ is the UV dust bump, parameterized using a Lorentzian-like Drude profile:

$$D(\lambda) = \frac{E_b(\lambda \Delta\lambda)^2}{(\lambda^2 - \lambda_0^2)^2 + (\lambda \Delta\lambda)^2} \quad (12)$$

where $\lambda_0 = 2175\text{\AA}$, $\Delta\lambda = 350\text{\AA}$, and $E_b = ?$ are the central wavelength, full width at half maximum, and strength of the bump, respectively. Once dust attenuation is applied to the SSPs, we sum them up to get the rest-frame luminosity of the galaxy. In total, our SPS model has 12 free parameters: M_* , 4 SFH basis coefficients, f_{burst} , t_{burst} , 2 ZH basis coefficients, τ_{BC} , τ_{ISM} , and n_{dust} .

In practice, evaluating each SSP using FSPS requires X seconds. For each model evaluation, we evaluate ~ 43 SSPs in each of the log-spaced t_{lookback} bins; this takes X seconds. Though this is not a prohibitive computational cost on its own, sampling a high dimensional parameter space for inference requires $> 100,000$ evaluations — *i.e.* > 100 CPU hours *per galaxy*. For the > 10 million BGS galaxies, this would require *a billion* CPU hours. Instead, we use an emulator for the model luminosity, which uses a Principal Component Analysis (PCA) neural network (NN) following the approach of Alsing et al. (2019).

TODO

TODO
TODOTODO
TODO

Table 1. Parameters of the PROVABGS SPS model used for joint SED modeling of DESI photometry and spectroscopy.

name	description	prior
$\log M_*$	log galaxy stellar mass	uniform over [8, 13]
$\beta_1, \beta_2, \beta_3, \beta_4$	NMF basis coefficients for SFH	Dirichlet prior
f_{burst}	fraction of total stellar mass formed in starburst event	uniform over [0, 1]
t_{burst}	time of starburst event	uniform over [10Myr, 13.2Gyr]
γ_1, γ_2	NMF basis coefficients for ZH	uniform over []
τ_{BC}	Birth cloud optical depth	uniform over []
τ_{ISM}	diffuse-dust optical depth	uniform over []
n_{dust}	? dust index	uniform over []
f_{fiber}	spectrum fiber-aperture effect normalization	Gaussian []

Our emulator consists of a NN and PCA basis functions. The NN provides a flexible and accurate mapping between the SPS model parameters and PCA coefficients — *i.e.* the NN predicts PCA coefficients for a given set of SPS parameters. Then the linear combination of the predicted coefficients and PCA basis functions give us the emulated model luminosity. The PCA basis functions and NN are trained using 1,000,000 pairs of SPS parameters and model luminosity, $(\theta, L(\lambda; \theta))$. Throughout the wavelength range relevant for BGS, $3000 < \lambda < 9800\text{\AA}$, we achieve $< 1\%$ accurate with the emulator. For details on the training, validation, and performance of our PCA NN emulator, we refer readers to Kwon *et al.* (in prep.).

From the rest-frame luminosity, we obtain the observed-frame, redshifted, flux in the same way as Eq. 2. In our case, redshift is not a free parameter since we will have spectroscopic redshifts for every DESI BGS galaxy. To model DESI photometry, we convolve the model flux with the LS broadband filters as in Eq. 3. To model DESI spectra, we first apply Gaussian velocity dispersion. In this work, we keep velocity dispersion fixed at 0km/s but in practice velocity dispersion can be set as a free parameter. Then the broadened flux is resampled into the wavelength binning of the observed DESI spectra, which has spectral resolution $R = 2000 - 5000$ over $3600 < \lambda < 9800\text{\AA}$. Since the DESI spectra does not necessarily include all the light of a galaxy, we include a nuisance parameter f_{fiber} , a normalization factor on the spectra to account for fiber aperture effects. Finally, the SPS model photometry and spectrum can be directly compared to observations.

TODO

3.2. Parameter Inference

Using the SPS model above, we perform Bayesian parameter inference to derive posterior probability distributions of the SPS parameters from photometry and spectroscopy. From Bayes rule, we write down the posterior as

$$p(\theta | \mathbf{X}) \propto p(\theta) p(\mathbf{X} | \theta) \quad (13)$$

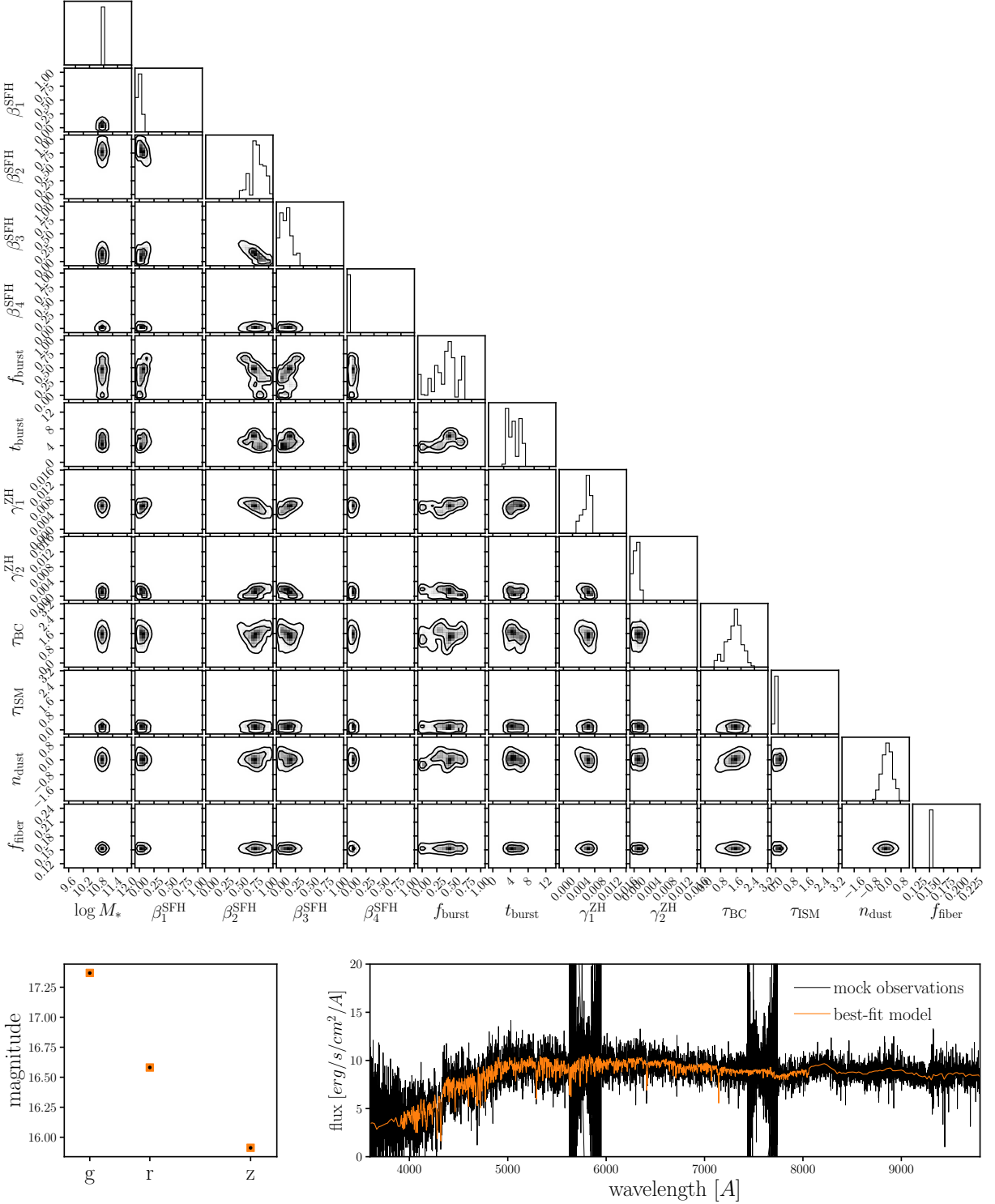


Figure 5. *Top:* Posterior probability distribution of our 12 SPS model parameters derived from joint SED modeling of the mock DESI photometry and spectrum. The contours mark the 68 and 95% percentiles. We use a Gaussian likelihood and the prior specified in Table 3.1 to evaluate the posterior and sample the distribution using ensemble slice MCMC. *With our Bayesian SED modeling approach, we capture the significant parameter degeneracies and multimodality of the posterior distribution.* *Bottom:* We compare the best-fit model observables (orange) to the mock observations (black). We find excellent agreement for both the LS photometry (left) and the DESI spectrum (right).

where \mathbf{X} is the photometry or spectrum and θ is the set of SPS parameters. $p(\mathbf{X} | \theta)$ is the likelihood, which we calculate separately for the photometry

$$\mathcal{L}^{\text{photo}} \propto \exp \left[-\frac{1}{2} \left(\frac{X^{\text{photo}} - m^{\text{photo}}(\theta)}{\sigma^{\text{photo}}} \right)^2 \right] \quad (14)$$

and for the spectrum

$$\mathcal{L}^{\text{spec}} \propto \exp \left[-\frac{1}{2} \left(\frac{X^{\text{spec}} - m^{\text{spec}}(\theta)}{\sigma^{\text{spec}}} \right)^2 \right]. \quad (15)$$

m^{photo} and m^{spec} represent SPS model for photometry and spectroscopy. σ^{photo} and σ^{spec} represent the uncertainties on the measured photometry and spectrum. We consider the photometry independent from the spectrum so we combine the likelihoods when jointly model the spectrophotometry:

$$\log \mathcal{L} \approx \log \mathcal{L}^{\text{photo}} + \log \mathcal{L}^{\text{spec}}. \quad (16)$$

$p(\theta)$ is the prior on the SPS parameters. For most of our parameters, we use uninformative uniform priors with conservatively chosen ranges that are listed in Table 3.1. However, for the priors of $\{\beta_1, \beta_2, \beta_3, \beta_4\}$, the NMF coefficients for the SFH, we use a Dirichlet distribution. With a Dirichlet distribution, β_i are within $0 < \beta_i < 1$ and satisfy the constraint $\sum_i \beta_i = 1$. This maintains the normalization of the SFH in Eq. 7.

Now that we can evaluate the posterior at given θ , we derive the posterior distributions using Markov Chain Monte Carlo (MCMC) sampling. We use the Karamanis & Beutler (2020) ensemble slice sampling MCMC algorithm with the ZEUS Python package. Ensemble slice sampling is an extension of standard slice sampling that does not require specifying the initial length scale or any further hand-tuning. Furthermore, it generally converges faster than other MCMC algorithms (*e.g.* Metropolis and standard slice sampling) and generates chains with significantly lower autocorrelation.

When we sample the posterior, we do not directly sample our 12 dimensional SPS parameter space. This is because we impose a Dirichlet prior on the SFH NMF coefficients. Dirichlet distributions are difficult to directly sample so we instead use the Betancourt (2012) sampling method, which transforms an N dimensional Dirichlet distribution into an easier to sample $N - 1$ dimensional space. Hence, we sample the posterior in the transformed 11 dimensional space. Given this dimensionality, we run our MCMC sampling with 30 walkers. Overall, we find that the sampling converges after 2,500 iterations with a 500 iteration burn in. Deriving the posterior distribution from a joint SED modeling of photometry and spectra, with the emulator, takes 0.5 CPU hours. In principle, since our emulator uses a PCA NN, we can further expedite our parameter inference using more efficient sampling methods that exploit gradient information, such as Hamiltonian Monte Carlo. We will explore further expediting our SED modeling in future works.

In Figure 3.1 we present the posterior distribution of our 12 SPS model parameters for an arbitrarily chosen LGAL mock observation. We mark the 68 and 95 percentiles of the distribution with the the contours. The posterior distribution reveal there are significant degeneracies between SPS parameters — *e.g.* β_2^{SFH} and f_{burst} . Furthermore, the distribution is multimodal (see f_{burst} panels). With our Bayesian SED modeling, we are able to capture such complexities in the posterior. In the

TODO

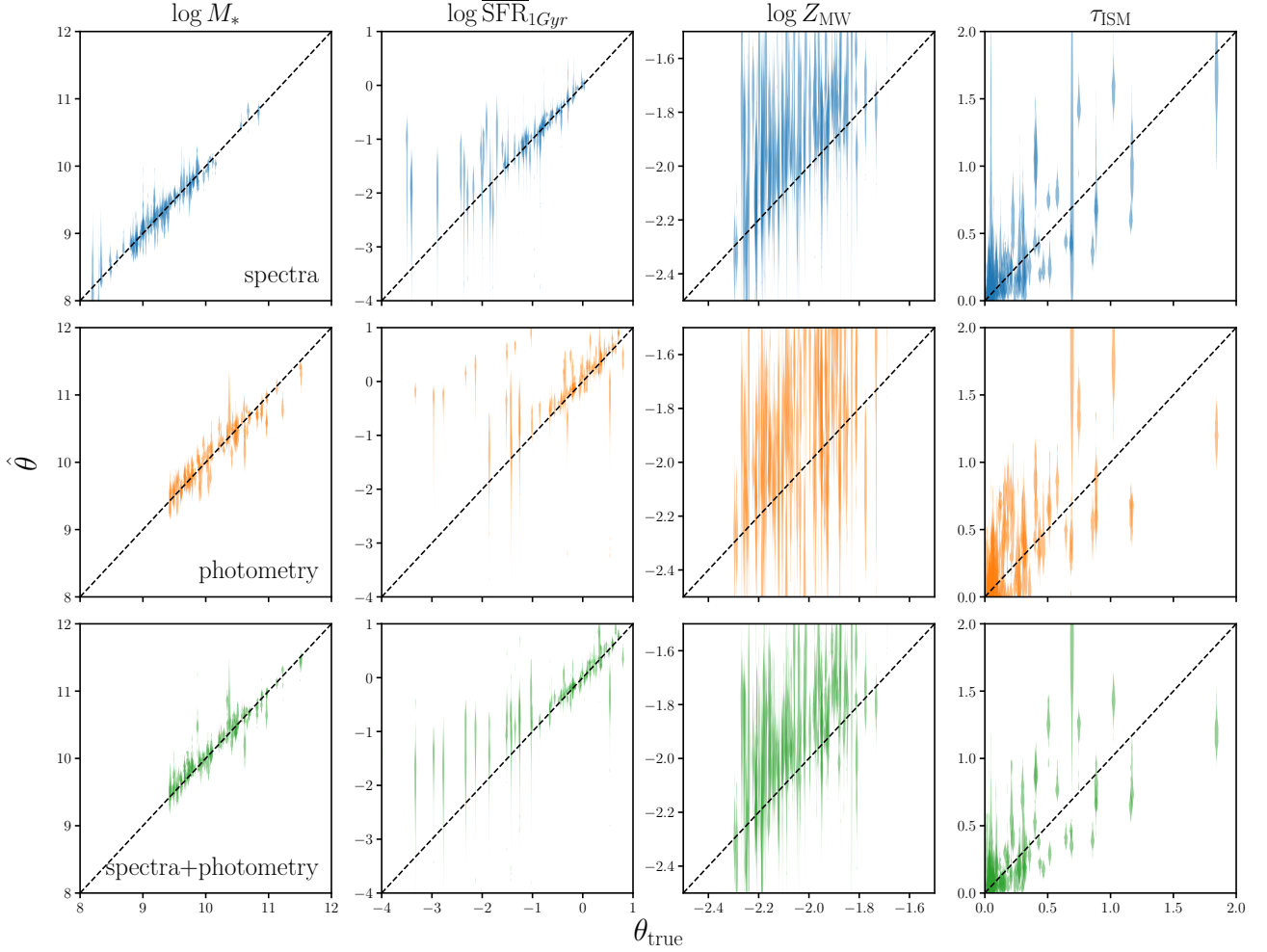


Figure 6. Comparison between the true galaxy properties, θ_{true} , and those inferred from SED modeling of mock observations, $\hat{\theta}$. From the left to right columns, we compare $\log M_*$, $\log \overline{\text{SFR}}_{1\text{Gyr}}$, $\log Z_{\text{MW}}$, and τ_{ISM} . The inferred galaxy properties are derived from SED modeling of mock spectra (top), photometry (middle), and spectra + photometry (bottom). For each simulated galaxy, we represent the marginalized posterior of θ with a violin plot.

bottom panels, we compare our SPS model evaluated at the best-fit parameters (orange) with the LGAL mock observations (black). On the left, we compare the g , r , z band magnitudes; on the right, we compare the DESI spectroscopy. We find excellent agreement between the best-fit SPS model and mock observations.

4. RESULTS

The goal of this work is to demonstrate the precision and accuracy of inferred galaxy properties for PROVABGS. We apply our SED modeling to the mock observables of 100 LGAL galaxies. From the posterior distributions of the SPS parameters, we derive the following physical galaxy properties: stellar mass (M_*), SFR averaged over 1 Gyr ($\overline{\text{SFR}}_{1\text{Gyr}}$), mass-weighted stellar metallicity (Z_{MW}), and diffuse-dust optical depth (τ_{ISM}). M_* and τ_{ISM} are both SPS model parameters. We derive $\overline{\text{SFR}}_{1\text{Gyr}}$

TODO

and Z_{MW} as

$$\overline{\text{SFR}}_{1\text{Gyr}} = \frac{\int_{t_{\text{age}}-1\text{Gyr}}^{t_{\text{age}}} \text{SFH}(t) dt}{1\text{Gyr}} \quad \text{and} \quad Z_{\text{MW}} = \frac{\int_0^{t_{\text{age}}} \text{SFH}(t) ZH(t) dt}{M_*}. \quad (17)$$

In Figure 6, we compare the galaxy properties inferred from SED modeling the mock observations, $\hat{\theta}$ to the true (input) galaxy properties, θ_{true} of the simulated galaxies. In each column, we compare $\log M_*$, $\log \overline{\text{SFR}}_{1\text{Gyr}}$, $\log Z_{\text{MW}}$, and τ_{ISM} from left to right. The inferred properties in the top, middle, and bottom rows are derived from SED modeling of spectra, photometry, and spectra + photometry, respectively. In each panel, we plot $\hat{\theta}$ using a violin plot, where the width of the marker represents the marginalized posterior distribution of θ . We note that in the comparison with SED modeling spectra only, we do not include f_{fiber} . Therefore, the true stellar mass in this case corresponds to $f_{\text{fiber}} \times M_*$. *Overall, the comparison demonstrates that we can robustly infer galaxy properties using the PROVABGS SED modeling.*

In more detail, we find that we infer unbiased and precise constraints on M_* throughout the entire M_* range. We also infer robust $\overline{\text{SFR}}_{1\text{Gyr}}$ for $\log \overline{\text{SFR}}_{1\text{Gyr}} > -2$ dex; below this limit, however, the inferred $\overline{\text{SFR}}_{1\text{Gyr}}$ are significantly less precise and overestimated the true $\overline{\text{SFR}}_{1\text{Gyr}}$. This bias at low $\overline{\text{SFR}}_{1\text{Gyr}}$ is caused by model priors, which we discuss in further detail later in [Section 5](#) and [Appendix A](#). Z_{MW} is not precisely constrained ($\sigma_{\log Z_{\text{MW}}} \sim 0.1$ dex); however, there is no strong bias in the constraints. Lastly, τ_{ISM} is accurately inferred for simulated galaxies with low τ_{ISM} but the accuracy declines significantly for high τ_{ISM} galaxies. TODO

The overall unbiased constraints on galaxy properties for the mock observations is especially encouraging due to the significant differences in the forward model used to generate the observations and the SPS model used in the SED modeling. First, the SFH in the forward model is taken directly from LGAL simulation outputs while the SFH parameterization in the SPS model is based on NMF bases fit to IllustrisTNG galaxy SFHs. Second, in the forward model, we construct the SED of the bulge and disk components of the simulated galaxies separately: the components have separate SFHs and ZHs. Lastly, we use different dust prescriptions: [Mathis \(1983\)](#) dust attenuation curve in the forward model and [Kriek & Conroy \(2013\)](#) dust attenuation curve in the SPS model. Despite these significant differences our constraints on galaxy properties are unbiased.

Figure 6, also highlights the advantages of jointly modeling spectra and photometry. Comparing the constraints from spectra+photometry to photometry alone, we find that including spectra significantly tightens the constraints for all properties. In addition to tightening constraints, including spectra also reduces the bias of the constraints. For instance, with only photometry, we derive biased $\overline{\text{SFR}}_{1\text{Gyr}}$ constraints for some of the galaxies. This is due to the limited constraining power of photometry, which allows the posteriors to be dominated by model priors. Adding spectra, significantly increases the contribution of the likelihood and ameliorates this effect.

We want to examine the precision and accuracy of the inferred galaxy properties beyond qualitative comparisons of the posteriors. Let $\Delta_{\theta,i}$ be the discrepancy between the inferred and true parameters for each galaxy: $\hat{\theta}_i = \theta_i^{\text{true}} + \Delta_{\theta,i}$. Then, if we assume that $\Delta_{\theta,i}$ are sampled from a

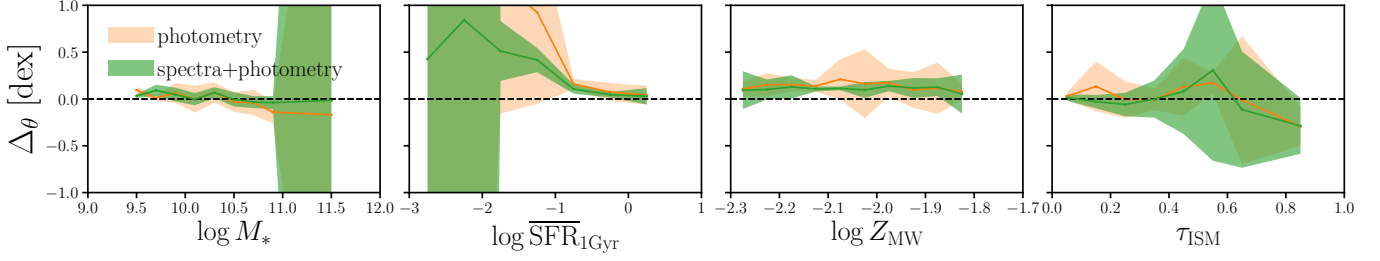


Figure 7. The accuracy and precision of our joint SED modeling of spectra+photometry, quantified using population hyperparameters $\mu_{\Delta\theta}$ and $\sigma_{\Delta\theta}$, as a function of true galaxy property (green). We plot $\mu_{\Delta\theta}$ in solid line and $\sigma_{\Delta\theta}$ in the shaded region. We include $\{\mu_{\Delta\theta}, \sigma_{\Delta\theta}\}$ for SED modeling of photometry alone (orange) for comparison.

Gaussian distribution,

$$\Delta_{\theta,i} \sim \mathcal{N}(\mu_{\Delta\theta}, \sigma_{\Delta\theta}), \quad (18)$$

the mean ($\mu_{\Delta\theta}$) and standard deviation ($\sigma_{\Delta\theta}$) of the distribution represent the accuracy and precision of the inferred posteriors for the galaxy population. Therefore, to quantify the bias and precision of our SED modeling, we derive the population hyperparameters ($\mu_{\Delta\theta}, \sigma_{\Delta\theta}$) using a hierarchical Bayesian framework (*e.g.* Hogg et al. 2010; ?; Baronchelli et al. 2020).

Let $\{\mathbf{X}_i\}$ represent the photometry or spectrum of a galaxy population and $\eta_{\Delta} = \{\mu_{\Delta\theta}, \sigma_{\Delta\theta}\}$ be the population hyperparameters. Our goal is to constrain η_{Δ} from $\{\mathbf{X}_i\}$ — *i.e.* $p(\eta_{\Delta} | \{\mathbf{X}_i\})$. As usual, we can expand

$$p(\eta_{\Delta} | \{\mathbf{X}_i\}) = \frac{p(\eta_{\Delta}) p(\{\mathbf{X}_i\} | \eta_{\Delta})}{p(\{\mathbf{X}_i\})} \quad (19)$$

$$= \frac{p(\eta_{\Delta})}{p(\{\mathbf{X}_i\})} \int p(\{\mathbf{X}_i\} | \{\theta_i\}) p(\{\theta_i\} | \eta_{\Delta}) d\{\theta_i\}. \quad (20)$$

θ_i is the SPS parameters for galaxy i and $p(\{\mathbf{X}_i\} | \{\theta_i\})$ is likelihood of the set of observations $\{\mathbf{X}_i\}$ given the set of $\{\theta_i\}$. Since the likelihoods for each of the N galaxies ($p(\mathbf{X}_i | \theta_i)$) are not correlated, we can factorize and write the expression above as

$$p(\eta_{\Delta} | \{\mathbf{X}_i\}) = \frac{p(\eta_{\Delta})}{p(\{\mathbf{X}_i\})} \prod_{i=1}^N \int p(\mathbf{X}_i | \theta_i) p(\theta_i | \eta_{\Delta}) d\theta_i \quad (21)$$

$$= \frac{p(\eta_{\Delta})}{p(\{\mathbf{X}_i\})} \prod_{i=1}^N \int \frac{p(\theta_i | \mathbf{X}_i) p(\mathbf{X}_i)}{p(\theta_i)} p(\theta_i | \eta_{\Delta}) d\theta_i \quad (22)$$

$$= p(\eta_{\Delta}) \prod_{i=1}^N \int \frac{p(\theta_i | \mathbf{X}_i) p(\theta_i | \eta_{\Delta})}{p(\theta_i)} d\theta_i. \quad (23)$$

$p(\theta_i | \mathbf{X}_i)$ is the posterior for an individual galaxy, so the integral can be estimated using the Monte Carlo samples from the posterior:

$$\approx p(\eta_\Delta) \prod_{i=1}^N \frac{1}{S_i} \sum_{j=1}^{S_i} \frac{p(\theta_{i,j} | \eta_\Delta)}{p(\theta_{i,j})}. \quad (24)$$

S_i is the number of posterior samples and $\theta_{i,j}$ is the j^{th} sample of galaxy i . In practice, $p(\theta_{i,j} | \eta_\Delta) = p(\Delta_{\theta,i,j} | \eta_\Delta)$ is a Gaussian distribution and, hence, easy to evaluate (Eq. 18). $p(\theta_{i,j}) = 1$ since we use uninformative and Dirichlet priors (Table 3.1). Lastly, we derive $p(\eta_\Delta | \{\mathbf{X}_i\})$ by sampling the distribution using MCMC.

In Figure 4, we present the accuracy and precision ($\mu_{\Delta_\theta}, \sigma_{\Delta_\theta}$) of our joint SED modeling of spectra and photometry (green) as a function of true galaxy property. We use the median of $p(\eta_\Delta | \{\mathbf{X}_i\})$ for μ_{Δ_θ} (solid) and σ_{Δ_θ} (shaded region). And in each panel, we derive $p(\eta_\Delta | \{\mathbf{X}_i\})$ for each property bin using the galaxies within it. We use bins with widths of 0.2, 0.2, 0.05, and 0.1 dex for $\log M_*$, $\overline{\text{SFR}}_{1\text{Gyr}}$, $\log Z_{\text{MW}}$, and τ_{ISM} respectively and only include bins with more than one galaxy. TODO

For $\log M_*$ and τ_{ISM} we find no bias in μ_{Δ_θ} even as a function of galaxy property. On the other hand, we confirm the significant bias in $\overline{\text{SFR}}_{1\text{Gyr}}$ at low $\overline{\text{SFR}}_{1\text{Gyr}} < -1$ dex: inferred $\overline{\text{SFR}}_{1\text{Gyr}}$ is biased by $\gtrsim 0.2$ dex at the SFRs. There is also a noticeable bias in $\log Z_{\text{MW}}$, which was difficult to detect in Figure 6. However, the bias is small compared to the precision ($\mu_{\Delta_\theta} \sim 0.1$ dex) and is independent of the true $\log Z_{\text{MW}}$.

The biases in $\overline{\text{SFR}}_{1\text{Gyr}}$ and $\log Z_{\text{MW}}$ are both a consequence of our SPS model priors (Appendix A). While $\log M_*$ and τ_{ISM} are directly parameters in our SPS model and, thus, have uniform priors. $\overline{\text{SFR}}_{1\text{Gyr}}$ and $\log Z_{\text{MW}}$, however, are derived quantities so the uniform priors we impose on SPS parameters induce non-uniform priors $\overline{\text{SFR}}_{1\text{Gyr}}$ and $\log Z_{\text{MW}}$. For our SPS model, we impose a prior on $\log \overline{\text{SSFR}}_{1\text{Gyr}}$ that is skewed and peaks at ~ -10.4 dex (Figure ??). Consequently, the posterior overestimates $\overline{\text{SFR}}_{1\text{Gyr}}$ at low $\overline{\text{SFR}}_{1\text{Gyr}}$. We also impose a skewed prior on $\log Z_{\text{MW}}$; however, the prior is significantly broader so the posteriors are only slightly biased.

In Figure 4, we also include $\{\mu_{\Delta_\theta}, \sigma_{\Delta_\theta}\}$ for SED modeling of photometry alone (orange). Comparing σ_{Δ_θ} , we confirm that including spectra significantly tightens the constraints on all of the galaxy properties. For instance, σ_{Δ_θ} for M_* improves from X to X dex once spectra is included. In addition to the increased precision, including spectra significantly improves the bias in the inferred galaxy properties. This is especially clear for $\overline{\text{SFR}}_{1\text{Gyr}}$, where the bias is reduced by X dex at $\overline{\text{SFR}}_{1\text{Gyr}} \sim -2$ dex. The bias on Z_{MW} is also noticeably reduced. Overall, Figure 4 illustrates that we derive over-all unbiased constraints on galaxy properties, except for low $\overline{\text{SFR}}_{1\text{Gyr}}$ galaxies, and that including spectra in the SED modeling substantially improves the inferred galaxy properties. TODO TODO

Beyond quantifying the accuracy and precision of our parameter inference as a function of galaxy properties, we examine how our parameter inference is impacted by signal-to-noise ratio (SNR) and photometric color. In Figure 8, we present η_Δ of our joint SED modeling of spectra and photometry as a function of r_{fiber} , r , $g - r$, and $r - z$. In each row, we plot η_Δ for a different galaxy property: $\log M_*$, $\overline{\text{SFR}}_{1\text{Gyr}}$, $\log Z_{\text{MW}}$, and τ_{ISM} (from top to bottom). r_{fiber} and r magnitudes serve proxies of the SNR for the spectra and photometry, respectively. Besides $\overline{\text{SFR}}_{1\text{Gyr}}$, we find no significant dependence

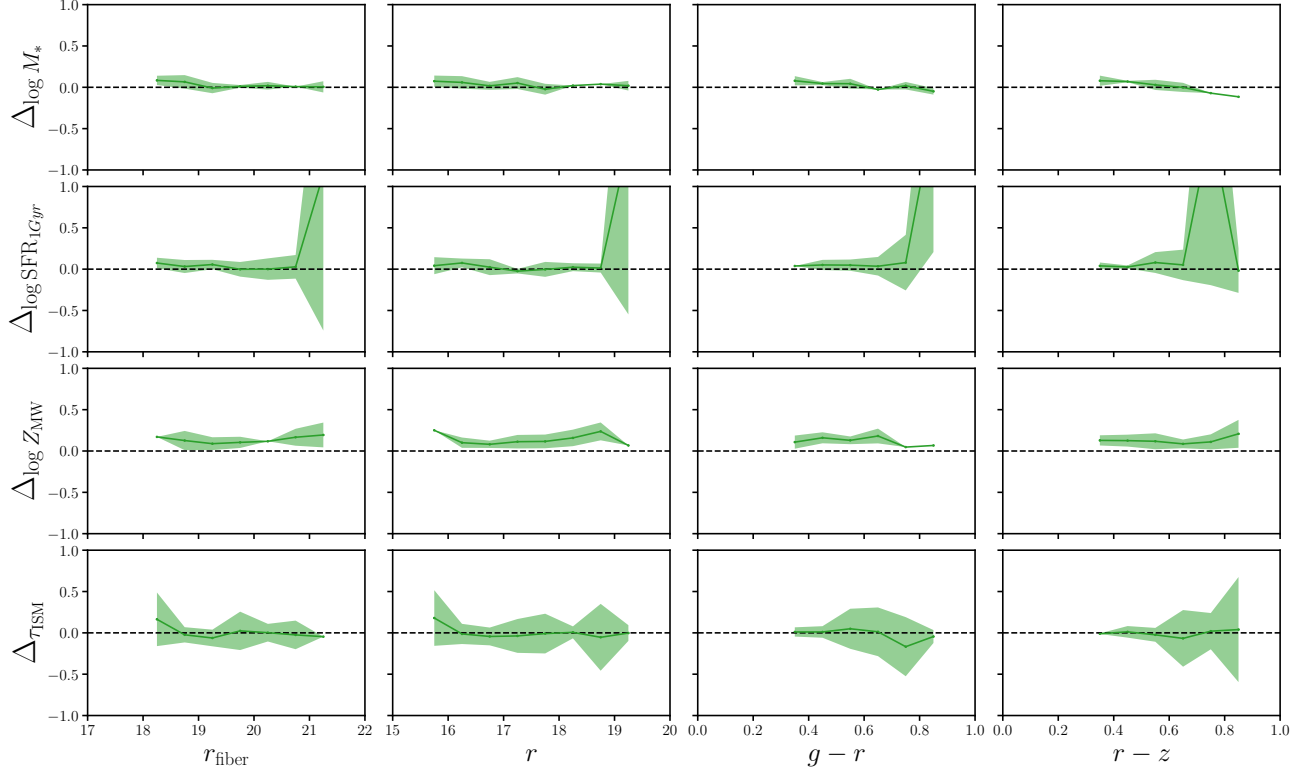


Figure 8. Accuracy and precision of the galaxy properties inferred from joint SED modeling of spectra+photometry as a function of r_{fiber} , r , $g-r$, and $r-z$. From the top to bottom rows, we present η_{Δ} for $\log M_*$, $\overline{\text{SFR}}_{1\text{Gyr}}$, $\log Z_{\text{MW}}$, and τ_{ISM} . r_{fiber} and r magnitudes are proxies for SNR of spectra and photometry. $g-r$ and $r-z$ are the optical photometric colors. We find no significant dependence on SNR or color in the accuracy of the inferred $\log M_*$, $\log Z_{\text{MW}}$, and τ_{ISM} .

on SNR or color in the inferred galaxy properties. We again confirm that the inferred M_* and τ_{ISM} values are unbiased. While the inferred Z_{MW} overestimate the true Z_{MW} , the bias is small ~ 0.1 dex and, more importantly, independent of SNR or color. Together with the results from Figure 4, we conclude that with our SED modeling we can infer robust constraints on M_* , Z_{MW} , and τ_{ISM} .

The situation is more complex for $\overline{\text{SFR}}_{1\text{Gyr}}$. For galaxies with high SNR spectra and photometry, we find no significant bias in the inferred $\overline{\text{SFR}}_{1\text{Gyr}}$. However, for $r_{\text{fiber}} > 20.5$ and $r > 19$, inferred $\overline{\text{SFR}}_{1\text{Gyr}}$ overestimates the true $\overline{\text{SFR}}_{1\text{Gyr}}$. color dependence once we get to the bottom of that

TODO

5. DISCUSSION

- restatement and discussion of robust galaxy property inference
- reiterate and discuss advantages of spectra+photometry that emphasizes why BGS will be awesome
- Beyond the galaxy properties we discuss in Section 4, we can also derive SFH and ZH
- posterior over MAP

- model priors and preview of how we can correct for it
- caveats: flux calibration — what was implemented versus what will need to be implemented in observations
- caveats: theoretical assumptions — isochrones and stellar libraries, summary of the appendix
- despite the caveats, this work demonstrates that the galaxy properties inferred will be robust and awesome. Paragraph that mentions the extension of all the previous science applications
- paragraph that discusses the new science applications with the posteriors.

6. SUMMARY

DESI is great.

Also advertise science papers with specific focus on mock challenge science papers.

ACKNOWLEDGEMENTS

It's a pleasure to thank Joel Leja, Peter Melchior ... This material is based upon work supported by the U.S. Department of Energy, Office of Science, Office of High Energy Physics, under contract No. DE-AC02-05CH11231. This project used resources of the National Energy Research Scientific Computing Center, a DOE Office of Science User Facility supported by the Office of Science of the U.S. Department of Energy under Contract No. DE-AC02-05CH11231.

APPENDIX

A. SPS MODEL PRIORS

B. SED MODELING UNCERTAINTIES FROM STELLAR EVOLUTION

REFERENCES

- Alsing J., et al., 2019, [arXiv:1911.11778 \[astro-ph\]](#)
- Baronchelli L., Nandra K., Buchner J., 2020, [Monthly Notices of the Royal Astronomical Society](#), 498, 5284
- Betancourt M. J., 2012, [arXiv:1010.3436 \[physics\]](#) 10.1063/1.3703631, pp 157–164
- Caplar N., Tacchella S., 2019, [arXiv:1901.07556 \[astro-ph\]](#)
- Carnall A. C., McLure R. J., Dunlop J. S., Davé R., 2017, [arXiv:1712.04452 \[astro-ph\]](#)
- Carnall A. C., Leja J., Johnson B. D., McLure R. J., Dunlop J. S., Conroy C., 2018, [arXiv:1811.03635 \[astro-ph\]](#)
- Chabrier G., 2003, [Publications of the Astronomical Society of the Pacific](#), 115, 763
- Charlot S., Fall S. M., 2000, [The Astrophysical Journal](#), 539, 718
- Choi J., Dotter A., Conroy C., Cantiello M., Paxton B., Johnson B. D., 2016, [The Astrophysical Journal](#), 823, 102
- Cichocki A., Phan A.-H., 2009, [IEICE Transactions on Fundamentals of Electronics Communications and Computer Sciences](#), 92, 708
- Conroy C., Gunn J. E., 2010, [The Astrophysical Journal](#), 712, 833
- Conroy C., Gunn J. E., White M., 2009, [The Astrophysical Journal](#), 699, 486
- Dey A., et al., 2019, [AJ](#), 157, 168

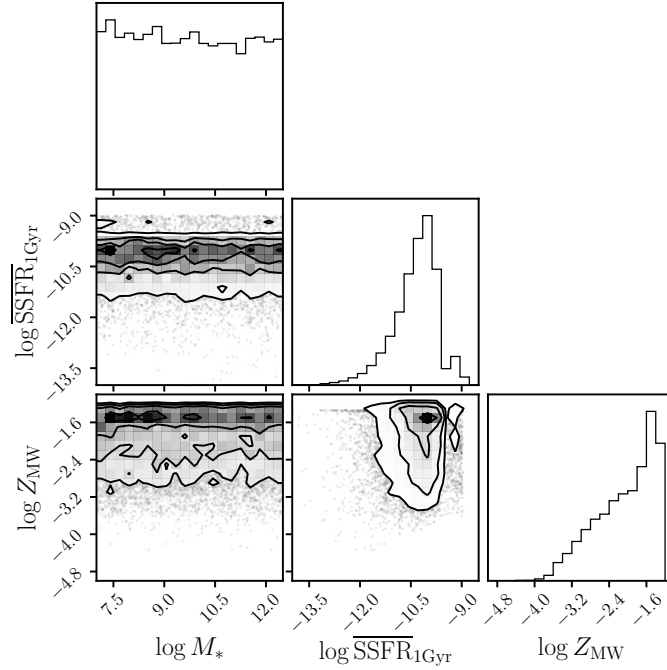


Figure 9. Priors imposed by our SPS model on $\log M_*$, $\log \overline{\text{SSFR}}_{1\text{Gyr}}$, and $\log Z_{\text{MW}}$ at $z = 0.1$.

- Dotter A., 2016, [The Astrophysical Journal Supplement Series](#), 222, 8
- Févotte C., Idier J., 2011, arXiv:1010.1763 [cs]
- Hahn C., Tinker J. L., Wetzel A., 2019, arXiv:1910.01644 [astro-ph]
- Henriques B. M. B., White S. D. M., Thomas P. A., Angulo R., Guo Q., Lemson G., Springel V., Overzier R., 2015, [Monthly Notices of the Royal Astronomical Society](#), 451, 2663
- Hogg D. W., Myers A. D., Bovy J., 2010, [The Astrophysical Journal](#), 725, 2166
- Iyer K. G., et al., 2020, [Monthly Notices of the Royal Astronomical Society](#), 498, 430
- Karamanis M., Beutler F., 2020, arXiv e-prints, p. arXiv:2002.06212
- Kriek M., Conroy C., 2013, [The Astrophysical Journal Letters](#), 775, L16
- Lee D. D., Seung H. S., 1999, [Nature](#), 401, 788
- Leja J., Johnson B. D., Conroy C., van Dokkum P. G., Byler N., 2017, [The Astrophysical Journal](#), 837, 170
- Leja J., Carnall A. C., Johnson B. D., Conroy C., Speagle J. S., 2019, [ApJ](#), 876, 3
- Mathis J. S., 1983, [The Astrophysical Journal](#), 267, 119
- Nelson D., et al., 2018, [Monthly Notices of the Royal Astronomical Society](#), 475, 624
- Paxton B., Bildsten L., Dotter A., Herwig F., Lesaffre P., Timmes F., 2011, [The Astrophysical Journal Supplement Series](#), 192, 3
- Paxton B., et al., 2013, [The Astrophysical Journal Supplement Series](#), 208, 4
- Paxton B., et al., 2015, [The Astrophysical Journal Supplement Series](#), 220, 15
- Pillepich A., et al., 2018, [Monthly Notices of the Royal Astronomical Society](#), 473, 4077
- Ruiz-Macias O., et al., 2021, [Monthly Notices of the Royal Astronomical Society](#), 502, 4328
- Serra P., Amblard A., Temi P., Burgarella D., Giovannoli E., Buat V., Noll S., Im S., 2011, [The Astrophysical Journal](#), 740, 22
- Simha V., Weinberg D. H., Conroy C., Dave R., Fardal M., Katz N., Oppenheimer B. D., 2014, arXiv e-prints, p. arXiv:1404.0402
- Sparre M., Hayward C. C., Feldmann R., Faucher-Giguère C.-A., Muratov A. L., Kereš D., Hopkins P. F., 2017, [Monthly Notices of the Royal Astronomical Society](#), 466, 88
- Springel V., et al., 2018, [Monthly Notices of the Royal Astronomical Society](#), 475, 676
- Tacchella S., et al., 2021, arXiv e-prints, 2102, arXiv:2102.12494
- Zahid H. J., Geller M. J., Fabricant D. G., Hwang H. S., 2016, [The Astrophysical Journal](#), 832, 203

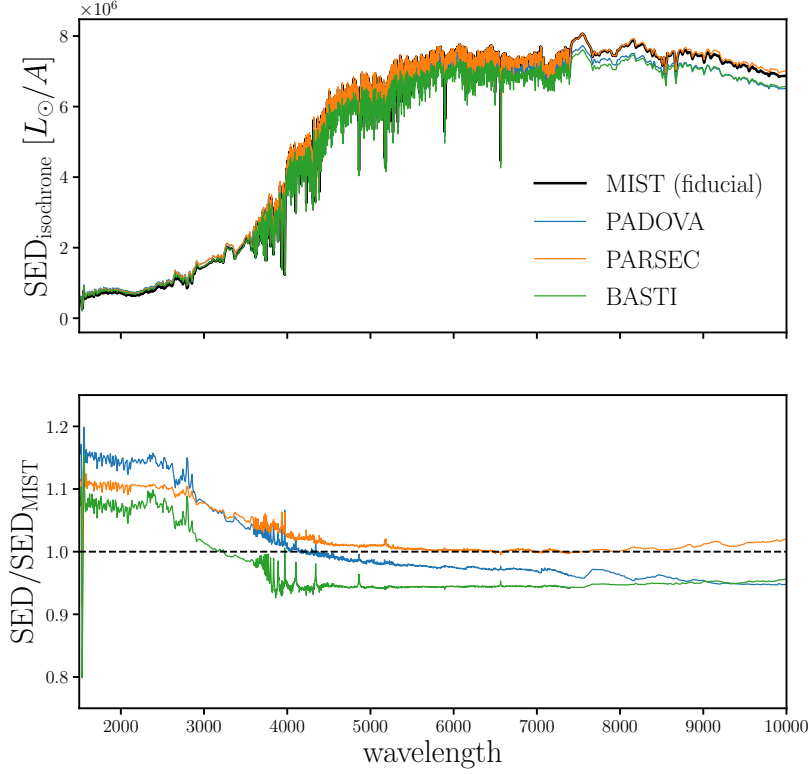


Figure 10. *Top:* Spectral energy distributions generated using MIST (black), Padova (blue), Parsec (orange), and BaSTI (green) isochrone libraries for an arbitrary set of SPS parameters. For our fiducial SED model, we use the MIST isochrone. *Bottom:* Ratios of the SEDs generated using different isochrone libraries over our fiducial MIST SED. The ratios reveal $> 10\%$ discrepancies at rest-frame UV wavelengths and significant offsets at higher wavelengths.

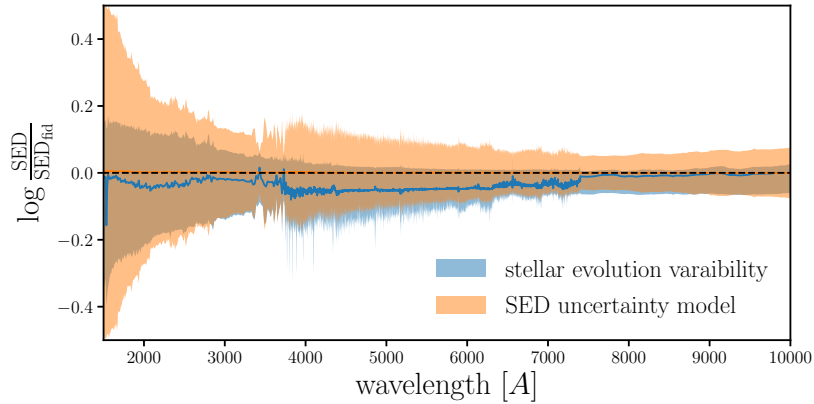


Figure 11.